Zhang et al. *Cell Discovery* (2024)10:40
https://doi.org/10.1038/s41421-024-00673-0

Cell Discovery
www.nature.com/celldisc

ARTICLE Open Access

Resistance mechanisms of SARS-CoV-2 3CLpro to the non-covalent inhibitor WU-04

Lijing Zhang[1,2,3,4], Xuping Xie[5], Hannan Luo[2,3,4], Runtong Qian[2,3,4], Yang Yang[6], Hongtao Yu[2,3,4,7], Jing Huang[2,3,4], Pei-Yong Shi[5]✉ and Qi Hu[2,3,4]✉

Abstract

Drug resistance poses a significant challenge in the development of effective therapies against SARS-CoV-2. Here, we identified two double mutations, M49K/M165V and M49K/S301P, in the 3C-like protease (3CLpro) that confer resistance to a novel non-covalent inhibitor, WU-04, which is currently in phase III clinical trials (NCT06197217). Crystallographic analysis indicates that the M49K mutation destabilizes the WU-04-binding pocket, impacting the binding of WU-04 more significantly than the binding of 3CLpro substrates. The M165V mutation directly interferes with WU-04 binding. The S301P mutation, which is far from the WU-04-binding pocket, indirectly affects WU-04 binding by restricting the rotation of 3CLpro's C-terminal tail and impeding 3CLpro dimerization. We further explored 3CLpro mutations that confer resistance to two clinically used inhibitors: ensitrelvir and nirmatrelvir, and revealed a trade-off between the catalytic activity, thermostability, and drug resistance of 3CLpro. We found that mutations at the same residue (M49) can have distinct effects on the 3CLpro inhibitors, highlighting the importance of developing multiple antiviral agents with different skeletons for fighting SARS-CoV-2. These findings enhance our understanding of SARS-CoV-2 resistance mechanisms and inform the development of effective therapeutics.

Introduction

The coronavirus 3C-like protease (3CLpro), also known as main protease (Mpro), plays a crucial role in processing two polyproteins (pp1a and pp1ab) encoded by the virus RNA genome[1]. Inhibiting the catalytic activity of 3CLpro has been proven to be an effective strategy to block coronavirus replication. Since the emergence of coronavirus disease 2019 (COVID-19)[2,3], caused by the SARS-CoV-2 virus, substantial efforts have been dedicated to the development of SARS-CoV-2 3CLpro inhibitors. Several 3CLpro inhibitors have been approved for treating COVID-19 patients, such as the covalent inhibitor PF-07321332 (nirmatrelvir)[4] and its analogs SIM0417 (simnotrelvir)[5], and RAY1216 (leritrelvir)[6]. A non-covalent inhibitor of 3CLpro, named S-217622 (ensitrelvir), has been approved in Japan for the treatment of COVID-19 patients[7].

With the increasing clinical use of 3CLpro inhibitors, the emergence of drug resistance has become a growing concern. Although no SARS-CoV-2 variants resistant to 3CLpro inhibitors have been reported in patients to date, several mutations in 3CLpro conferring resistance to nirmatrelvir have been identified through in vitro studies[8–19]. According to the crystal structure of the 3CLpro/nirmatrelvir complex (PDB code: 7RFS)[4], most of these mutation sites are located at three segments within 5 Å of nirmatrelvir, including residues 140–144, 163–168, and 186–192. Mutations in these segments either directly disrupt their interactions with nirmatrelvir or alter the conformation of the nirmatrelvir-binding pocket, thus leading to drug resistance[18,20]. There are also mutations that target residues located far away from nirmatrelvir, such as T21I, P252L, and T304I. Although each of these mutations contributes a modest level of resistance, they

Correspondence: Pei-Yong Shi (peshi@utmb.edu) or
Qi Hu (huqi@westlake.edu.cn)
[1]Zhejiang University, Hangzhou, Zhejiang, China
[2]Westlake Laboratory of Life Sciences and Biomedicine, Hangzhou, Zhejiang, China
Full list of author information is available at the end of the article
These authors contributed equally: Lijing Zhang, Xuping Xie.

are thought to act as initial mutations that facilitate the emergence of additional ones, leading to robust resistance to nirmatrelvir. However, the precise mechanisms by which these mutations confer resistance remain to be elucidated[10].

All clinically approved inhibitors of SARS-CoV-2 3CLpro are designed to target the substrate-binding pocket of 3CLpro, which raises concern about cross-resistance. Many of the nirmatrelvir-resistant mutations also confer resistance to ensitrelvir[16–19]. However, mutations that confer resistance to one drug but not the other have also been reported. For example, the A173V mutation significantly reduces the potency of nirmatrelvir, but has minimal impact on the potency of ensitrelvir[17]. In contrast, mutations at M49, such as M49I and M49L, show little impact on the potency of nirmatrelvir but result in substantial resistance to ensitrelvir[17,18]. Understanding the spectrum of drug resistance presented by 3CLpro inhibitors that have varying scaffolds and binding modes is crucial for addressing potential cross-resistance issues.

We recently reported the development of a novel class of non-covalent inhibitors targeting coronavirus 3CLpro[21]. Among them, WU-04 demonstrated significant potency towards 3CLpro in the original SARS-CoV-2 strain (wild-type, WT) and the Omicron variants. It also effectively inhibited other coronaviruses, such as SARS-CoV and MERS-CoV[21]. Now, WU-04 is undergoing phase III clinical trials for the treatment of COVID-19 (NCT06197217). In this study, we have identified mutations in SARS-CoV-2 3CLpro that confer resistance to WU-04. By determining their crystal structures, we have elucidated the mechanisms for WU-04 resistance. Additionally, we studied mutations that confer resistance to ensitrelvir and nirmatrelvir, and assessed the cross-resistance of 3CLpro carrying these mutations to WU-04, ensitrelvir and nirmatrelvir.

Results

Mutations in 3CLpro confer SARS-CoV-2 resistance to WU-04

Having identified the potent anti-SARS-CoV-2 inhibitor WU-04, we sought to explore the possibility of developing WU-04-resistant mutations in SARS-CoV-2. Selection of the resistant virus was performed in African green monkey kidney epithelial Vero E6 cells using a reporter SARS-CoV-2 (this virus showed significantly reduced virulence in vivo compared to the WT SARS-CoV-2). WU-04 blocked SARS-CoV-2 replication in Vero E6 cells with half-maximal inhibitory concentration (IC_{50}) value of 10–20 nM. By serially passaging the reporter SARS-CoV-2 in Vero E6 cells in the presence of increasing concentrations of WU-04, we identified four strains of SARS-CoV-2 that could survive 10 μM WU-04 (Supplementary Fig. S1a). Two strains carried double nucleotide mutations T10200A (3CLpro: M49K) and A10547G (3CLpro: M165V) in the viral genomes, whereas the other two strains carried double mutations T10200A (3CLpro: M49K) and T10955C (3CLpro: S301P). Fortunately, the three-drug resistance mutations were found in the GISAID database (https://gisaid.org/) with a relatively low frequency (Supplementary Table S1).

In the crystal structure of the SARS-CoV-2 3CLpro/WU-04 complex, residues M49 and M165 pack against the bromophenyl ring of WU-04, suggesting that these mutations directly hinder the binding of WU-04 to 3CLpro (Fig. 1a). The identification of resistant mutations in the WU-04-binding pocket of 3CLpro validates the on-target effect of WU-04 in cellular assays. Residue S301 is located at the end of the last α-helix of 3CLpro. It precedes the C-terminal tail (residues 301–306), which is involved in 3CLpro homodimerization (Fig. 1a). The S301P mutation may indirectly impede WU-4 binding through modulating the C-terminal tail of 3CLpro.

We purified the WT 3CLpro and the WU-04-resistant mutants and measured their inhibition by WU-04 using a fluorescence-based enzyme assay (Fig. 1b). Both the M49K and M165V mutations increased the IC_{50} of WU-04 against 3CLpro by more than 20-fold. Combination of the two mutations further increased the IC_{50} to greater than 10 μM. The S301P mutation alone slightly increased the IC_{50}, but in combination with the M49K mutation, drastically increased the IC_{50} to greater than 5 μM.

We then measured the binding affinities of these 3CLpro mutants to WU-04 using isothermal titration calorimetry (ITC). Consistent with the decreased sensitivity of these mutants to WU-04, the dissociation constants (K_d) for these mutants bound to WU-04 were all increased (Fig. 1c; Supplementary Fig. S1b). Interestingly, though the M49K/S301P mutant showed stronger WU-04 resistance than the M165V mutant, its binding affinity to WU-04 was higher than that of the M165V mutant, indicating a resistant mechanism beyond the decreased WU-04 binding.

We next evaluated the effects of these mutations on the catalytic activity of SARS-CoV-2 3CLpro (Fig. 1d). The protease activities of each mutant at different substrate concentrations were measured to obtain the V_{max}, K_m and k_{cat}, and calculate the k_{cat}/K_m ratio as a measurement of the catalytic activity. All these mutants showed higher K_m and lower k_{cat} value in comparison with the WT 3CLpro. Specifically, the k_{cat}/K_m ratios of the double mutants, M49K/M165V and M49K/S301P, were only about one fifth and one seventh of that of the WT 3CLpro, respectively. These results demonstrate that there is a trade-off between the catalytic activity and the WU-04 resistance of 3CLpro. The reduction in k_{cat} could potentially be

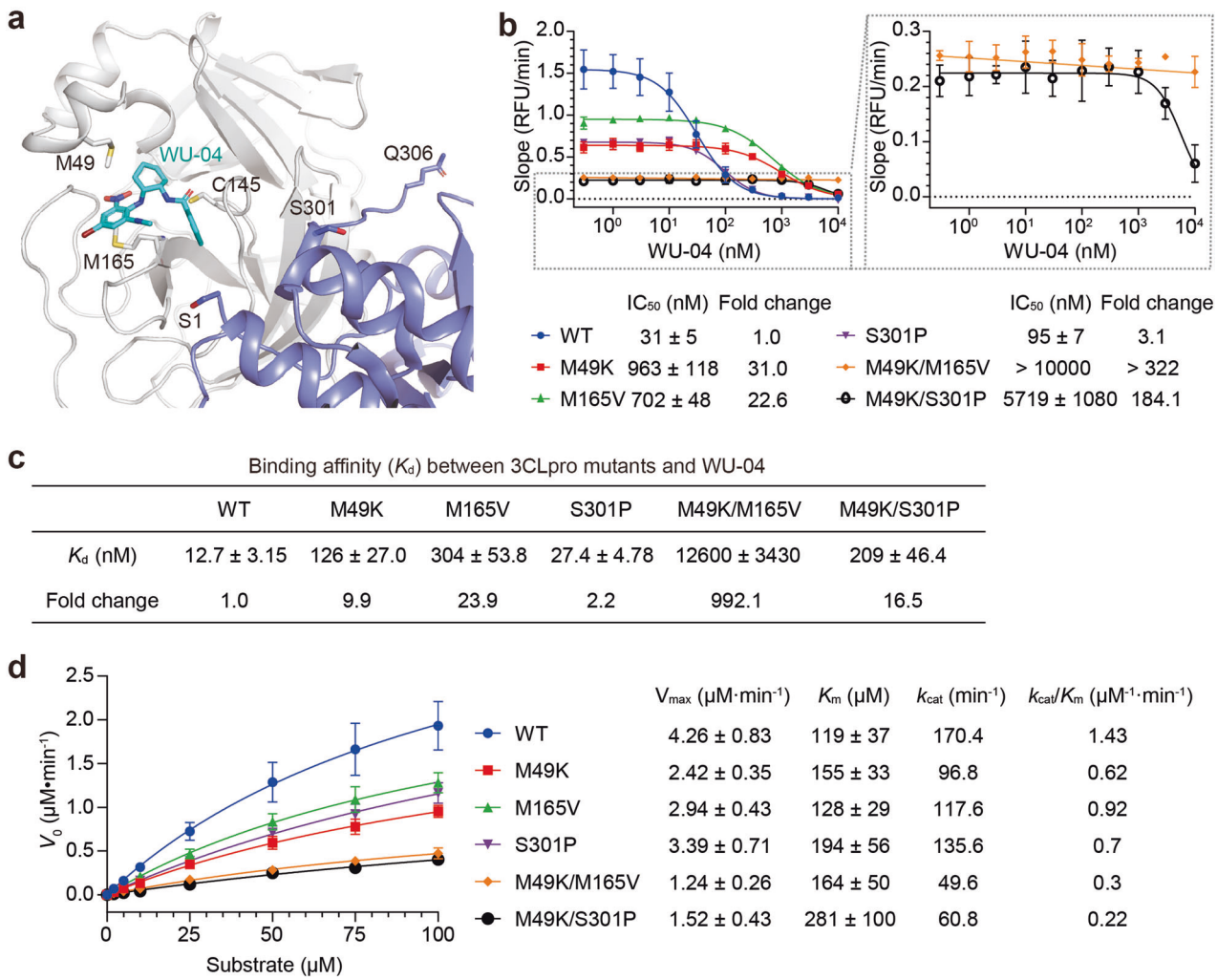

Fig. 1 Characterization of WU-04-resistant mutations in SARS-CoV-2. a The crystal structure of the WT SARS-CoV-2 3CLpro in complex with WU-04 (PDB code: 7EN8). Two double mutations M49K/M165V and M49K/S301P of SARS-CoV-2 3CLpro were identified as WU-04-resistant mutations. Residues M49, M165, and the catalytic residue C145 from one 3CLpro protomer (colored gray), along with residue S301 and the N- and C-terminal residues S1 and Q306 from the other 3CLpro protomer (colored slate) within the same 3CLpro homodimer, are depicted as sticks in the crystal structure. **b** The inhibitory activity of WU-04 against the SARS-CoV-2 3CLpro mutants was assessed using a FRET-based assay. The two double mutants M49K/M165V and M49K/S301P showed the strongest resistance to WU-04. The data represent the means ± SD of three independent measurements. **c** The binding affinity (K_d) between WU-04 and each 3CLpro mutant was measured using isothermal titration calorimetry (ITC), and then normalized to that between WU-04 and the WT 3CLpro to obtain the fold change value. **d** The catalytic activity of each 3CLpro mutant was evaluated using the FRET-based assay. The data of V_{max} and K_m represent the means ± SD of three independent measurements. The k_{cat} values were calculated by dividing the mean values of V_{max} by the concentration of 3CLpro (25 nM) in the assay system.

attributed to either a disturbance within the catalytic site or a destabilization of the 3CLpro dimer.

The M49K mutation disturbs the substrate-binding pocket of 3CLpro

To understand how these mutations affect the WU-04 sensitivity and the catalytic activity of 3CLpro, we solved the crystal structures of these mutants (Supplementary Table S2) and aligned them with the crystal structure of the WT 3CLpro. The overall structures of these mutants are very similar to that of the WT 3CLpro (PDB code: 6M03), with RMSD values below 0.4 Å.

In the crystal structure of the M49K mutant, three regions around the substrate-binding pocket show conformational changes in comparison with the structure of the WT 3CLpro (Fig. 2a). One is the short helix (residues 45–51) in which the M49K mutation is located. The electron density of this helix in the crystal structure of the M49K mutant is so weak that its structure cannot be modeled (Supplementary Fig. S2a, b), indicating that the M49K mutation

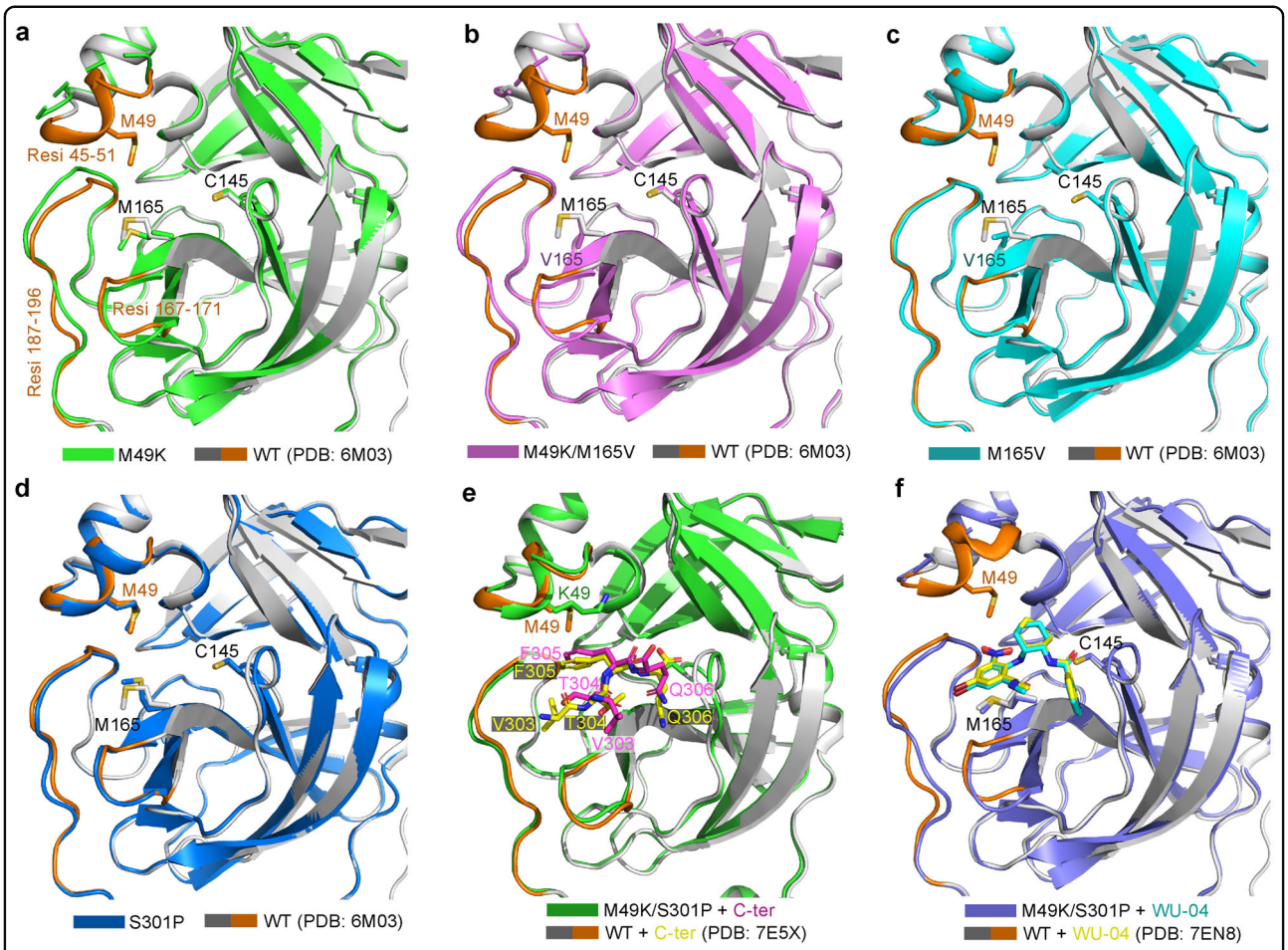

Fig. 2 The WU-04-resistant mutation M49K perturbs the substrate-binding pocket of SARS-CoV-2 3CLpro. a–d Alignment of the crystal structures of the WU-04-resistant SARS-CoV-2 3CLpro mutants M49K (**a**), M49K/M165V (**b**), M165V (**c**), and S301P (**d**) with the crystal structure of the WT 3CLpro (PDB code: 6M03). **e** Alignment of the crystal structure of the double mutant M49K/S301P with that of the WT 3CLpro in the post-cleavage state (PDB code: 7E5X). The C-terminal tail from another molecule of 3CLpro in the M49K/S301P structure and that in the WT 3CLpro structure were shown as sticks and colored magentas and yellow, respectively. **f** Alignment of the crystal structure of the double mutant M49K/S301P in complex with WU-04 with the crystal structure of the WT 3CLpro in complex with WU-04 (PDB code: 7EN8). WU-04 in the M49K/S301P structure and that in the WT 3CLpro structure are colored cyan and yellow, respectively. Three regions in the WT 3CLpro, including a short helix where M49 is located (residues 45–51), a short loop (residues 167–171), and the linker connecting domains II and III of 3CLpro (residues 187–196), are colored brown in the crystal structure. Each alignment was carried out by aligning the structure of one protomer of each 3CLpro mutant with the structure of one protomer of the WT 3CLpro using the "align" command in PyMol.

destabilizes this short helix. The other two regions are the loop (residues 167–171) after M165 and the linker (residues 187–196) connecting domains II and III of 3CLpro. Both show slight conformational changes upon introducing the M49K mutation. Conformational changes in the three regions are also observed in the crystal structure of the M49K/M165V double mutant (Fig. 2b; Supplementary Fig. S2c), but not in the crystal structure of the M165V mutant (Fig. 2c; Supplementary Fig. S2d) or that of the S301P mutant (Fig. 2d). These structures demonstrate that the M49K mutation disturbs the local structure around the substrate-binding pocket of 3CLpro, but the M165V mutation does not induce conformational changes.

Unexpectedly, residues 45–51 in the crystal structure of the M49K/S301P double mutant have good electron density (Supplementary Fig. S2e) and the conformation is similar to that in the structure of the WT 3CLpro. Structural analysis revealed that the C-terminus of one molecule of the M49K/S301P double mutant was docked into the substrate-binding pocket of another molecule of this mutant (Fig. 2e), thus this structure may represent the post-cleavage state of the M49K/S301P double mutant. Alignment of this structure with the crystal structure of the WT 3CLpro in the post-cleavage state (PDB code: 7E5X) shows that the two structures are almost identical to each other, except that residues V303 and T304 from the C-terminus of another molecule of 3CLpro have

different orientations in the substrate-binding pockets (Fig. 2e). We have also solved the crystal structure of the M49K/S301P double mutant in complex with WU-04 and found that residues 45–51 have poor electron density (Fig. 2f; Supplementary Fig. S2f), similar to that in the M49K structure. The conformation and binding position of WU-04 in this structure are the same as that in the crystal structure of the WT 3CLpro/WU-04 complex (PDB code: 7EN8). These findings suggest that the conformation of residues 45–51 altered by the M49K mutation can be stabilized by binding to 3CLpro substrates but not WU-04. Thus, the M49K mutation has a greater effect on WU-04 binding than on 3CLpro substrate binding.

The S301P mutation restricts the rotation of the C-terminal tail of 3CLpro

In contrast to the M49K and M165V mutations, which directly affect the catalytic activity of 3CLpro and inhibit 3CLpro binding, the S301P mutation affects a residue located far from the WU-04 binding site. S301 is located at the end of the last helix of 3CLpro. In the crystal structure of the mature WT 3CLpro (PDB code: 6M03), the C-terminal tail (residues 301–306) of each 3CLpro molecule binds to the other 3CLpro molecule in the same 3CLpro homodimer (Fig. 3a, b), but in the M49K/S301P and S301P structures this C-terminal tail is oriented towards a different direction so that it is no longer involved in 3CLpro dimerization (Fig. 3c, d; Supplementary Fig. S3a). In the crystal structure of the WT 3CLpro in the post-cleavage state (PDB code: 7E5X), the C-terminal tails of the two 3CLpro molecules in each 3CLpro homodimer have distinct orientations (Fig. 3e; Supplementary Fig. S3c, d): the one (chain A) that represents the post-cleavage state of 3CLpro docks into the substrate-binding pocket of 3CLpro in another 3CLpro homodimer, in an orientation similar to that in the M49K/S301P structure; while the other (chain B) is involved in 3CLpro homo-dimerization, with its orientation being similar to that in the structure of the mature WT 3CLpro (PDB code: 6M03). The different orientations are caused by the rotation of the backbone Φ angle of S301 (Fig. 3e). We speculate that, after cleavage, the C-terminal tail of 3CLpro switches from the post-cleavage state (chain A) to the mature state (chain B) to stabilize the 3CLpro homodimer.

When S301 is mutated to a proline residue, the Φ angle of P301 is fixed. Consequently, the C-terminal tail cannot be rotated and is restricted to a conformation that cannot contribute to the homo-dimerization of 3CLpro (Fig. 3f; Supplementary Fig. S3b, e, f). This finding indicates that the S301P mutation destabilizes the homodimers of 3CLpro.

To validate this finding, we measured the K_d values for the WT and mutant 3CLpro to form homodimers using mass photometry (MP)[22] (Table 1; Supplementary Fig. S4). The S301P mutant showed a significantly decreased dimerization ability ($K_d = 17.81 \pm 7.32$ nM) compared to the WT 3CLpro ($K_d = 0.94 \pm 0.21$ nM). In contrast, mutations M49K and M165V did not inhibit 3CLpro dimerization.

In addition, we carried out 100-ns molecular dynamics (MD) simulations for the homodimers of both the WT 3CLpro and the S301P mutant, and analyzed the free energies (ΔG) between two 3CLpro monomers with the molecular mechanics/generalized Born surface area (MM/GBSA) method using the final 90 ns of the MD trajectories. The ΔG value changed from −124.75 kcal/mol with the WT system to −103.90 kcal/mol with the S301P system, indicating that the 3CLpro homodimer is destabilized by the S301P mutation. Decomposition of the ΔG into different components suggested that electrostatic interactions accounted for the majority (69.7%) of the weakened interaction.

Drug resistance mutations decrease the catalytic activity and destabilize 3CLpro

We also studied the mutations that make 3CLpro resistant to other two inhibitors: the non-covalent inhibitor ensitrelvir and the covalent inhibitor nirmatrelvir, with the aim of understanding the similarities and differences between these mutations. Initially, we focused on the impact of these mutations on the catalytic activity and thermostability of 3CLpro.

The substrate-binding pocket of 3CLpro can be divided into four sites: S1', S1, S2, and S4 according to the interactions between 3CLpro and its peptide substrates[23]. In contrast to WU-04, which occupies the S1, S2 and S4 sites of the substrate-binding pocket of 3CLpro (Fig. 4a, d), ensitrelvir occupies the S1, S1' and S2 sites (Fig. 4b, e). Nirmatrelvir also occupies S1, S2 and S4 (Fig. 4c, f), but the specific interactions with 3CLpro differ from those observed with WU-04. A few mutations in 3CLpro have been reported to confer resistance to ensitrelvir; among them, mutations at M49 of 3CLpro showed the strongest effects[17,24]. We chose M49I as a representative mutation. Additionally, we analyzed the crystal structure of 3CLpro in complex with ensitrelvir (PDB code: 7VU6) and found that the side chain of T25 was in close proximity to the methylindazol ring of ensitrelvir (Fig. 4e). Therefore, we also selected the T25I and T25V mutations as potential ensitrelvir-resistant mutations. For nirmatrelvir, resistance mutations or deletions at nearly all residues within the nirmatrelvir-binding pocket have been reported[8–12,16,17,25]. We selected the mutations and deletions that have been reported to confer strong resistance to nirmatrelvir.

All mutants were recombinantly expressed in *E. coli* and purified to homogeneity. The k_{cat}/K_m ratio of each mutant

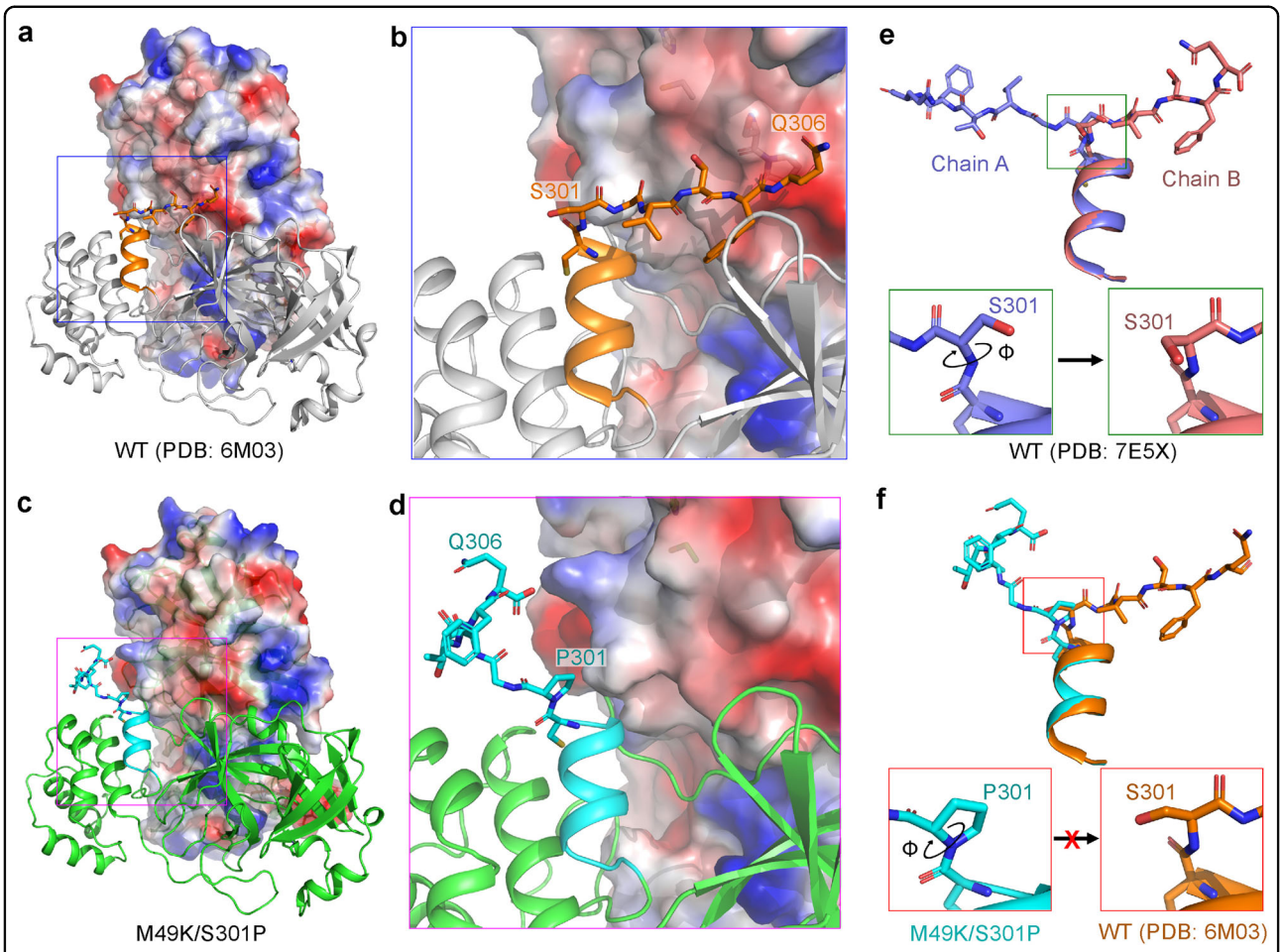

Fig. 3 The S301P mutation locks the C-terminal tail of 3CLpro in the post-cleavage state. a, **b** In the crystal structure of the WT 3CLpro in the mature state (PDB code: 6M03), the C-terminal tail (residues 301–306, shown in sticks and colored orange) of one 3CLpro protomer binds to the other 3CLpro protomer (the protein contact potential was calculated using PyMOL) within the same 3CLpro homodimer. **c**, **d** In the crystal structure of the M49K/S301P double mutant, the C-terminal tail (colored cyan) of one 3CLpro protomer turns away from the other 3CLpro protomer within the same 3CLpro homodimer. **e** Alignment of the C-terminal tails of the two 3CLpro protomers (colored purple and salmon, respectively) within the same 3CLpro homodimer in the crystal structure of the WT 3CLpro in the post-cleavage state (PDB code: 7E5X). The two C-terminal tails have distinct orientations. Rotation of the Φ angle of S301 switches the C-terminal tail from the post-cleavage state (chain A) to the mature state (chain B). **f** Alignment of the C-terminal tails of 3CLpro in the M49K/S301P structure (colored cyan) with that in the mature WT 3CLpro structure (colored orange). In the M49K/S301P mutant, the Φ angle of P301 is fixed, and therefore, the C-terminal tail of 3CLpro is locked at the post-cleavage state.

Table 1 The homodimer dissociation constants (K_d) of the WT SARS-CoV-2 3CLpro and its mutants measured using mass photometry.

SARS-CoV-2 3CLpro	K_d for dimerization (nM)
WT	0.94 ± 0.21
M49K	0.69 ± 0.15
M165V	0.43 ± 0.15
S301P	17.81 ± 7.32
M49K/M165V	0.83 ± 0.19
M49K/S301P	10.93 ± 1.37

was calculated and normalized to that of the WT 3CLpro (Fig. 4g; Supplementary Fig. S5). All these mutants, except L50F, showed decreased catalytic activities. In comparison with 3CLpro mutants that are resistant to the non-covalent inhibitors WU-04 and ensitrelvir, most of the nirmatrelvir-resistant mutants exhibited much lower catalytic activities. For the E166V, L50F/E166V, H172Y, H163W and M165Y mutants, as well as 3CLpro with Q189 or Q192 deletions (ΔQ189 and ΔQ192), their activities in our assay were so low that their V_{max} and K_m values could not be determined and were therefore labeled as not detectable (ND).

It is notable that the L50F mutant demonstrated higher activity as compared to the WT 3CLpro: the k_{cat}/K_m ratio

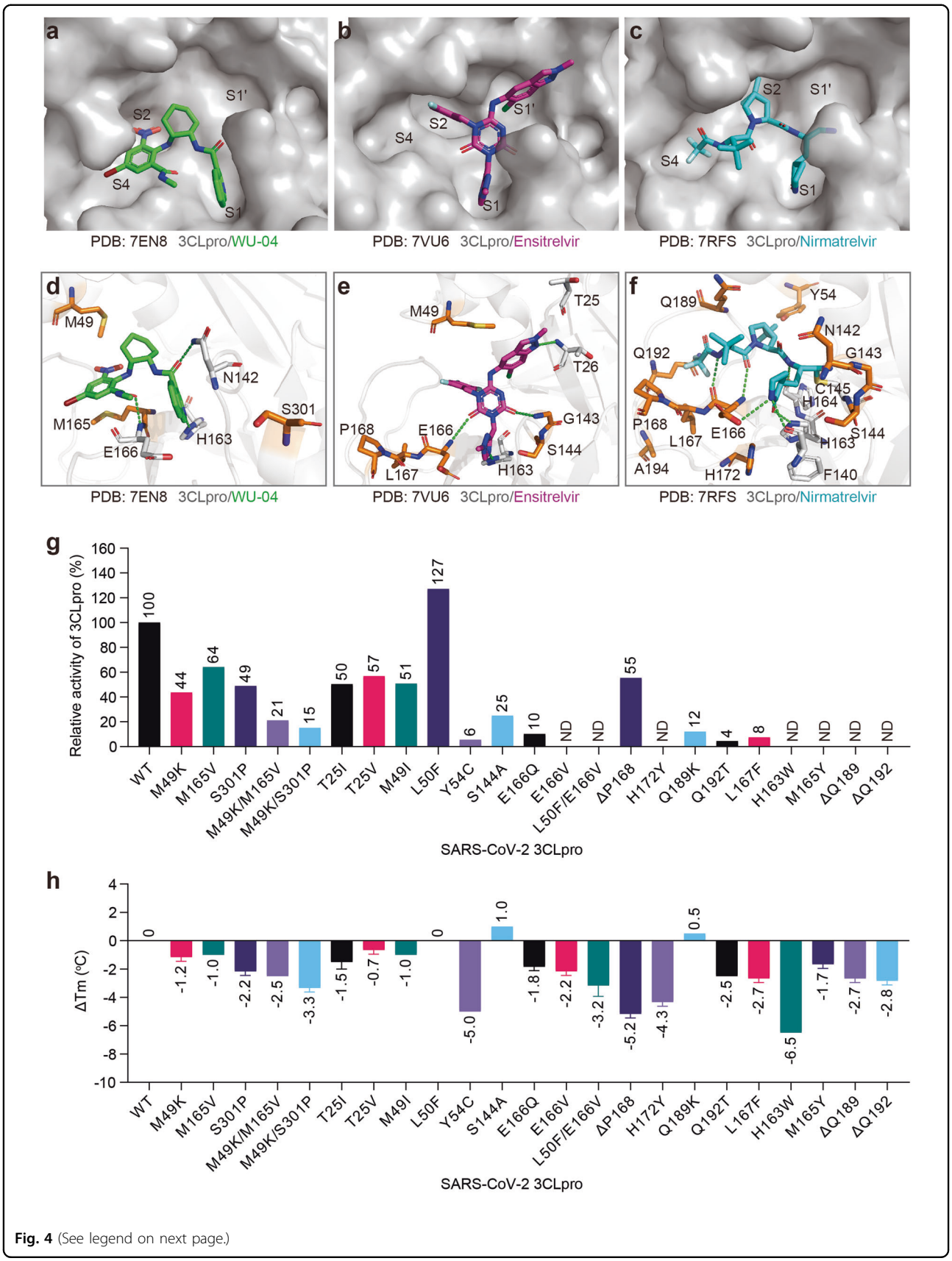

Fig. 4 (See legend on next page.)

(see figure on previous page)

Fig. 4 3CLpro mutations that confer resistance to WU-04, ensitrelvir and nirmatrelvir decreased the catalytic activity and thermostability of 3CLpro. a–c Occupancy of the substrate-binding pocket of SARS-CoV-2 3CLpro by the non-covalent inhibitors WU-04 (**a**) and ensitrelvir (**b**), and the covalent inhibitor nirmatrelvir (**c**). **d–f** Interactions between SARS-CoV-2 3CLpro and WU-04 (**d**), between SARS-CoV-2 3CLpro and ensitrelvir (**e**), and between SARS-CoV-2 3CLpro and nirmatrelvir (**f**). Hydrogen bonds are indicated by green dash lines. The residue mutations that may confer resistance to the three inhibitors are colored orange. **g** Relative catalytic activities of the drug-resistant 3CLpro mutants. The catalytic activity (k_{cat}/K_m) of each mutant was evaluated using a FRET-based assay with three independent measurements, and then normalized to that of the WT 3CLpro. **h** Changes in the melting temperature (T_m) of SARS-CoV-2 3CLpro induced by drug resistance mutations. The T_m of each mutant was evaluated using a thermal shift assay. The data represent the means ± SD of technical triplicate.

of the L50F mutant was 1.82 μM^{-1} min^{-1}, higher than that of the WT 3CLpro (1.43 μM^{-1} min^{-1}). This observation is distinct from that in previous studies in which the catalytic activity of the L50F mutant was reported as only 0.1% or 0.4% of that of the WT 3CLpro[9,11]. The L50F mutation also enhanced the catalytic activity of the El66V mutant (Supplementary Fig. S5c).

We also evaluated the impact of these drug resistance mutations on the thermostability of 3CLpro by using a thermal shift assay[26]. Nearly all these mutations or deletions resulted in a decrease in the melting temperature (T_m) of 3CLpro (Fig. 4h; Supplementary Fig. S6). Among them, the Y54C mutation, P168 deletion (ΔP168), and H163W mutation decreased the T_m of 3CLpro by a minimum of 5 °C. In contrast, three mutations, L50F, S144A, and Q189K, displayed no effect or led to a slight increase in the T_m of 3CLpro.

Cross-resistance of purified 3CLpro mutants to non-covalent and covalent inhibitors

We subsequently assessed the inhibitory activities of WU-04, ensitrelvir, and nirmatrelvir against purified 3CLpro using the fluorescence-based enzyme assay. For the non-covalent inhibitors WU-04 and ensitrelvir, their IC_{50} values against each mutant were determined (Supplementary Fig. S7) and normalized to the IC_{50} values against the WT 3CLpro (Fig. 5a). For the covalent inhibitor nirmatrelvir, the inhibition constant (K_i) against each mutant was calculated (Supplementary Fig. S8), following the method described previously[4], and normalized to that against the WT 3CLpro (Fig. 5a).

For the WU-04-resistant mutants that were identified in our study, they also exhibited differing levels of resistance to ensitrelvir and nirmatrelvir, although the degree of resistance was not as notable as that observed towards WU-04 (Fig. 5a). Specifically, the IC_{50} values of ensitrelvir against the M49K, M165V, and S301P mutants were 2.8, 3.3, and 1.7 times that against the WT 3CLpro, respectively. The double mutants M49K/M165V and M49K/S301P exhibited stronger resistance to ensitrelvir as compared to these single mutants: the IC_{50} values are 10.2 and 7.8 times that against the WT 3CLpro, respectively. An increase in the K_i of nirmatrelvir was also observed, particularly for the S301P and M49K/S301P mutants.

For the three mutants, including T25I, T25V and M49I, that were selected as ensitrelvir-resistant mutants, the IC_{50} values of ensitrelvir against them were 3.2, 5.7, and 4.5 times that against the WT 3CLpro, respectively (Fig. 5a). In contrast, these mutants exhibited negligible resistance to WU-04 and nirmatrelvir. The M49I mutant became even more sensitive to WU-04, with an IC_{50} value approximately half of that against the WT 3CLpro (Supplementary Fig. S7a).

Among the fifteen mutants selected for nirmatrelvir resistance, the catalytic activities of seven were too low to be accurately determined in the enzyme assay. The drug resistance of the remaining eight mutants were evaluated (Fig. 5a). Six mutants, including Y54C, S144A, E166Q, Q192T, L167F, and ΔP168, demonstrated strong resistance to all three inhibitors. The Q189K mutant exhibited moderate resistance to WU-04, but no resistance to ensitrelvir or nirmatrelvir. The L50F mutant was not resistant to any of the three inhibitors.

Cross-resistance of 3CLpro mutants expressed in HEK 293 T cells to non-covalent and covalent inhibitors

The purified WT 3CLpro and its mutants underwent N- and C-terminal cleavage, thus representing the mature state of 3CLpro. In order to simulate the self-cleavage process of 3CLpro during coronavirus replication, we developed a bioluminescence resonance energy transfer (BRET)-based self-cleaving biosensor pBRET-10, in which a green fluorescent protein (GFP2) and a Renilla luciferase (RLuc8) were linked to the N- and C-termini of SARS-CoV-2 3CLpro, respectively, using linkers derived from the cleavage sequences of 3CLpro[27]. BRET from RLuc8 to GFP2 can be disrupted by self-cleavage and preserved if the self-cleavage is inhibited. The biosensors carrying the WT 3CLpro and a chosen set of 3CLpro mutants were transiently expressed in human embryonic kidney (HEK) 293T cells. Then the cells were treated with serial dilutions of the inhibitors, and the BRET signals were measured (Supplementary Fig. S9). The IC_{50} of each inhibitor against each 3CLpro mutant was calculated and normalized to that against the WT 3CLpro (Fig. 5b).

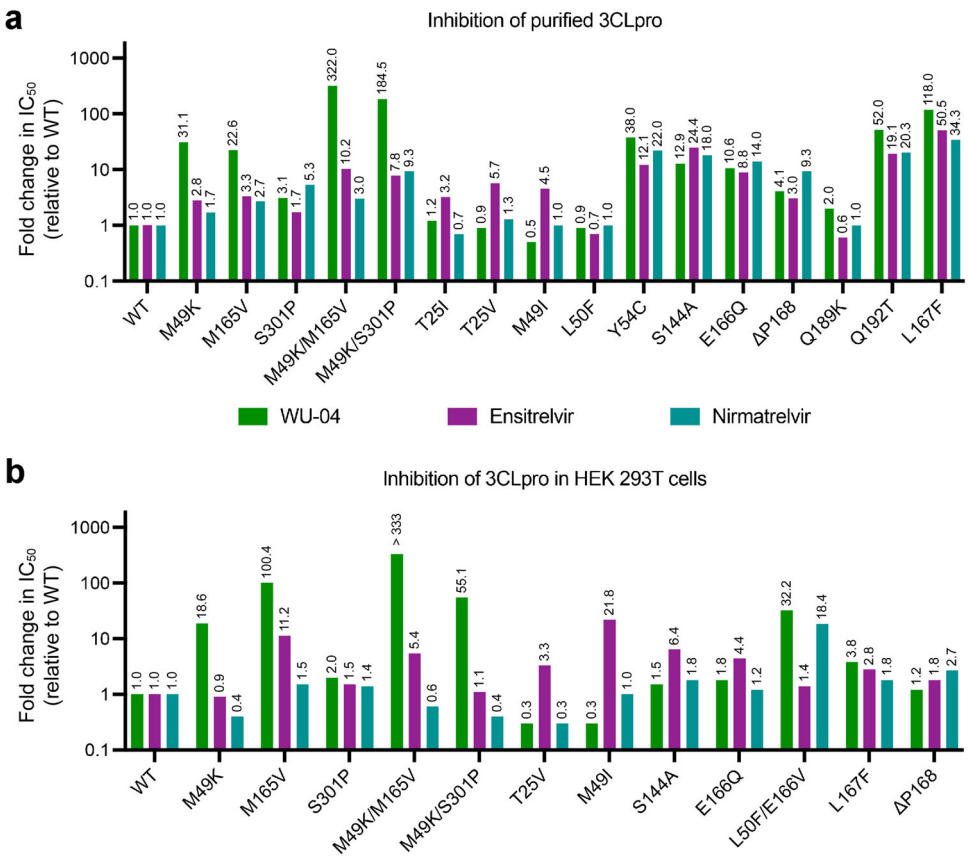

Fig. 5 Cross-resistance of 3CLpro mutants to WU-04, ensitrelvir and nirmatrelvir. a, **b** The IC_{50} of WU-04, ensitrelvir and nirmatrelvir against the WT 3CLpro and its mutants were evaluated using a fluorescence-based enzyme assay (**a**), and a BRET-based cell assay (**b**). Each IC_{50} value was calculated based on the data from three independent experiments, then normalized to the IC_{50} value of the corresponding compound against the WT 3CLpro to obtain the fold change value.

Four mutants that exhibited strong resistance to WU-04 in the enzyme assay, including the M49K, M165V, M49K/M165V, and M49K/S301P mutants, also exhibited strong resistance to WU-04 in the cell assay (Fig. 5b). However, the ranking of resistance levels is different from that in the enzyme assay. Particularly, the M165V mutant demonstrated greater resistance to WU-04 than the M49K and M49K/S301P mutants in the cell assay, whereas its resistance level was lower than that of the M49K and M49K/S301P mutants in the enzyme assay. The M165V mutant also showed greater resistance to ensitrelvir, while the M49K and M49K/S301P mutants showed negligible resistance to ensitrelvir (Fig. 5b). The activity of nirmatrelvir against the four mutants was either moderately affected or even surpassed that against the WT 3CLpro (Fig. 5b).

The T25V and M49I mutants, which exhibited ensitrelvir resistance in the enzyme assay, were also resistant to ensitrelvir in the cell assay, with the respective IC_{50} values 3.3 and 21.8 times that against the WT 3CLpro. Conversely, the two mutants exhibited increased sensitivity to WU-04, with their IC_{50} values decreased to ~30% of that against the WT 3CLpro (Fig. 5b); this observation aligns with the findings from the enzyme assay.

Three mutants, S144A, E166Q, and L167F, showed moderate resistance to all the three inhibitors in the cell assay, in contrast to their strong resistance against the three inhibitors in the enzyme assay (Fig. 5b). Among them, S144A and E166Q showed greater resistance to ensitrelvir than to WU-04 and nirmatrelvir. Another mutant, Δ168, exhibited moderate resistance to all three inhibitors (Fig. 5b).

The double mutant L50F/E166V, which showed remarkably weak activity in the enzyme assay, exhibited strong resistance to WU-04 and nirmatrelvir, with the IC_{50} values 32.2 and 18.4 times that against the WT 3CLpro, respectively (Fig. 5b). In contrast, it exhibited negligible resistance to ensitrelvir (Fig. 5b).

Discussion

We have identified two double mutants of 3CLpro, M49K/M165V and M49K/S301P, that exhibit resistance to the non-covalent inhibitor WU-04. The three

mutations in these double mutants each uniquely impact the structure and function of 3CLpro and confer different levels of resistance to WU-04.

Both M49 and M165 are situated within 5 Å of WU-04 (Fig. 1a); mutations at the two residues substantially decrease the binding affinity between 3CLpro and WU-04 (Fig. 1c). The M49K mutation disturbs three regions in 3CLpro (Fig. 2a). Particularly, this mutation destabilizes the short helix of 3CLpro containing residues 45–51, resulting in alterations to the conformation of the WU-04-binding pocket and thereby explaining the resistance to WU-04. In contrast, the crystal structure of the M165V mutant is almost identical to that of the WT 3CLpro (Fig. 2c). M165, located within a β-strand deep within the WU-04-binding pocket, when mutated to the branched-chain amino acid valine, may cause a clash with the bromophenyl ring of WU-04, directly impeding WU-04 binding.

Compared to the M49K and M165V mutations, the S301P mutation had a moderate effect on the binding affinity between 3CLpro and WU-04 (Fig. 1c) and only caused a slight increase in the IC_{50} of WU-04 (Fig. 1b). However, when combined with the M49K mutation, the S301P mutation significantly increased the IC_{50} of WU-04 (Fig. 1b). The S301P mutation restricts the rotation of the C-terminal tail of 3CLpro, thereby perturbing the dimerization of 3CLpro (Fig. 3; Table 1). This unique resistance mechanism is different from those of the M49K and M165V mutations. The S301P mutation was also identified in the screening for nirmatrelvir-resistant mutations[10]. We confirmed that it conferred resistance to nirmatrelvir (Fig. 5a). This observation indicates that restriction of the rotation of the C-terminal tail of 3CLpro serves as a resistance mechanism for nirmatrelvir as well.

Alongside the WU-04-resistant mutations, we also investigated mutations and deletions that confer resistance to ensitrelvir and nirmatrelvir. Almost all of these alterations resulted in a decrease in the catalytic activity of 3CLpro (Fig. 4g). Specific mutations, including E166V, L50F/E166V, H172Y, H163W, M165Y, ΔQ189, and ΔQ192, significantly reduced the catalytic activity of 3CLpro to almost undetectable levels (Fig. 4g; Supplementary Fig. S5). Most of these mutations also decreased the thermostability of 3CLpro (Fig. 4h). These findings suggest a trade-off between the catalytic activity, thermostability and drug resistance of 3CLpro. However, even with low levels of 3CLpro protease activity, viral replication can still be sustained, as evidenced by the high fitness of the virus carrying either the L50F/E166V double mutation or the L50F/E166A/L167F triple mutation in 3CLpro[11,28], suggesting that nearly complete inhibition is needed to block viral replication.

An unexpected finding is that the L50F mutation, previously reported to significantly decrease the catalytic activity of 3CLpro[9,11], actually enhanced the catalytic activity of 3CLpro (Fig. 4g; Supplementary Fig. S5). Our finding aligns with the observation that the L50F mutation compensated for the replicative fitness loss caused by the E166V mutation[10,11]. A yeast screen also indicated that the L50F mutation can increase the catalytic activity of 3CLpro, however, there was a lack of enzymatic assay data[19]. A recent study showed that the double mutant L50F/E166V had increased catalytic activity compared to the E166V single mutant, indicating that the L50F mutation increased the 3CLpro catalytic activity[20]. The controversy over the catalytic activity of the L50F mutant may be due to the difficulty in obtaining a well-behaved, purified sample of this mutant in previous studies. We successfully expressed and purified the L50F mutant, thus presenting conclusive evidence of its increased catalytic activity. This finding suggests that the decreased catalytic activity of 3CLpro caused by most of the drug resistance mutations can be restored by introducing additional mutations.

A number of mutations, such as Y54C, S144A, E166Q, Q192T, and L167F, confer robust resistance to all three inhibitors. However, certain mutants exhibit resistance to one inhibitor while remaining sensitive to others, as exemplified by mutations at M49 (Fig. 5). In enzyme assays, the M49K mutation significantly increased the IC_{50} of WU-04, but only moderately affected the potency of ensitrelvir and nirmatrelvir; conversely, the M49I mutation had minimal impact on the potency of WU-04 and nirmatrelvir but caused a significant increase in the IC_{50} of ensitrelvir (Fig. 5a). In our cell-based assay that was designed to evaluate the self-cleavage efficiency of 3CLpro, the M49K mutation resulted in a nearly 20-fold increase in the IC_{50} of WU-04 but had negligible effect on the efficacy of ensitrelvir (Fig. 5b). In contrast, the M49I mutation caused a nearly 20-fold increase in the IC_{50} of ensitrelvir but decreased the IC_{50} of WU-04 (Fig. 5b). These findings demonstrate that mutations at the same residue can have distinct effects on the 3CLpro inhibitors. This underscores the importance of developing multiple antiviral agents with different skeletons for fighting SARS-CoV-2.

We used two assays to evaluate the resistance conferred by 3CLpro mutations: an enzyme assay using purified, mature 3CLpro, and a cell assay using a biosensor to mimic the maturation process of 3CLpro in HEK 293T cells. Interestingly, these two assays yielded different rankings of resistance levels for the 3CLpro mutations. For instance, while the L167F mutation conferred stronger resistance to WU-04 than the M49K and M165V mutations in the enzyme assay, it demonstrated much weaker resistance in the cell assay. This discrepancy potentially suggests that the inhibitory activity varies between mature and unprocessed 3CLpro. However, the precise molecular mechanisms underpinning this difference remain to be elucidated.

The limitation of the current study is that we have not analyzed the roles of individual mutations in the context of full-length SARS-CoV-2 in viral fitness and their contributions to antiviral drug resistance.

Materials and methods

Selection and sequencing of WU-04-resistant virus

The WU-04-resistant virus was obtained by serial passaging of the SARS-CoV-2 mNG (this virus showed significantly reduced virulence in vivo compared to the WT SARS-CoV-2)[29] in Vero E6 cells in the presence of increasing concentrations of WU-04. Four selections for WU-04-resistant virus were independently performed. Briefly, a reporter virus, named SARS-CoV-2 mNG, was generated by introducing the gene of mNeonGreen into ORF7 of the SARS-CoV-2 viral genome[30]. For each selection, Vero E6 cell monolayers in a 12-well plate were inoculated at a multiplicity of infection (MOI) of 2 with SARS-CoV-2 mNG or previously passaged virus and the compound. After incubation at 37 °C for 1 h, the inoculum was removed, and 1 mL fresh DMEM medium with 2% FBS containing WU-04 was added to each well. The cell cultures were incubated at 37 °C for 2–5 days. The culture medium was harvested when over 80% of cells showed mNG-positive. Selection began at the WU-04 concentration of 120 nM (P1) and was followed by increasing the WU-04 concentrations to 480 nM (P2), 2000 nM (P3), 4000 nM (P4), and 10,000 nM (P5-P7). The supernatant from 10,000 nM WU-04-selected virus (P7) was tested for WU-04 sensitivity on Vero CCL81 cells. For viral genome sequencing, viral RNA was extracted from P7 culture fluids by using the TRIzol™ LS Reagent (ThermoFisher Scientific), and the cDNA fragment containing the nucleotides 7382–11,990 in the SARS-CoV-2 genome was amplified by using SuperScript™ IV One-Step RT-PCR System (ThermoFisher Scientific). The RT-PCR products were purified and subjected to Sanger sequencing. The selection process for the WU-04-resistant viruses was conducted during the early stage of COVID-19 pandemic, before any antiviral drugs, including nirmatrelvir, which had been authorized for emergency use. During the selection process, WU-04 resistant viruses exhibited comparable replication kinetics to the SARS-CoV-2 mNG strain. The selected viruses had only been tested for their sensitivity to WU-04. No other antiviral inhibitors have been tested using these resistant viruses. All virus experiments were conducted at Biosafety level-3 laboratories. Personnel who performed the experiments wore powered air-purifying respirators (Breathe Easy, 3 M) with Tyvek suits, aprons, booties, and double gloves.

Genes and cloning

The gene coding the SARS-CoV-2 3CLpro was a gift from Prof. Sheng-ce Tao at Shanghai Jiao Tong University. The plasmid of SARS-CoV-2 3CLpro (WT) for protein expression and BRET assay were reported in our previous studies[21,27]. The plasmids of SARS-CoV-2 3CLpro mutants were constructed through QuickChange site-directed mutagenesis by using ClonExpress® II One Step Cloning Kit (Vazyme, C112-02).

Protein expression and purification

The SARS-CoV-2 3CLpro proteins were overexpressed in *Escherichia coli* and purified following a method described previously[21]. In brief, the His-tagged proteins were purified by affinity chromatography using Co^{2+} resin (TALON, 635504), then the tag was removed by human rhinovirus 3C protease (TaKaRa, 7360) and the efficiency of cleavage was analyzed by SDS-PAGE (GenScript, M00656). The proteins were further purified by ion-exchange chromatography (Source-15Q column, GE Healthcare) and size-exclusion chromatography (Superdex 200 increase 10/300 GL column, GE Healthcare). Finally, the purified proteins were concentrated and stored in 20 mM HEPES, pH 7.4, 150 mM NaCl at −80 °C for subsequent biological assays and crystallization.

3CLpro FRET-based assay

The enzymatic activities of the WT 3CLpro and its mutants, and the inhibitory activity of each inhibitor (WU-04, Ensitrelvir, and Nirmatrelvir) were evaluated using a fluorescence resonance energy transfer (FRET)-based assay as described previously[21]. The fluorogenic peptide Dabcyl-KTSAVLQSGFRKME-Edans was used as the substrate.

For the enzyme kinetic study, the final concentration of 3CLpro was 25 nM. In detail, 20 μL of 3CLpro (50 nM) in the reaction buffer (20 mM HEPES 7.4, 150 mM NaCl, 0.01% Triton X-100, 1 mM DTT) was added into a 384-well black plate (Corning, CLS3575) and incubated at 37 °C for 5 min, then 20 μL of different concentrations (0–200 μM) of the fluorogenic substrate in the reaction buffer was added to each well to initiate the reaction. The fluorescence was monitored at 37 °C using an excitation wavelength of 355 nm and an emission wavelength of 538 nm in a Thermol Varioskan LUX plate reader. A control experiment containing only the fluorogenic substrate in the reaction was carried out. A standard curve was generated using the product (SGFRKME-Edans), then the fluorescence signals of each sample were converted to the product concentrations. The slope of each curve from 0 to 10 min was calculated as the velocity of the corresponding reaction. Three independent experiments were performed. The data were fitted by the software GraphPad Prism 9 using the Michaelis-Menten equation to obtain the V_{max} and K_m values of the WT 3CLpro and its mutants.

To measure the IC_{50} values of WU-04 and Ensitrelvir, the final concentration of 3CLpro was 25 nM. Specially,

10 μL of each inhibitor at a series of concentrations in the dilution buffer (20 mM HEPES 7.4, 150 mM NaCl, 0.01% Triton X-100, 1 mM DTT, 10% DMSO) was incubated with 10 μL of 3CLpro (100 nM) in the reaction buffer (20 mM HEPES 7.4, 150 mM NaCl, 0.01% Triton X-100, 1 mM DTT) at room temperature for 30 min and then incubated at 37 °C for 5 min. Next, 20 μL of the fluorogenic substrate (50 μM) in the reaction buffer was added to each well to initiate the reaction. The fluorescence was monitored at 37 °C with an excitation wavelength of 355 nm and an emission wavelength of 538 nm using a Thermol Varioskan LUX plate reader. A control experiment containing inhibitors and the fluorogenic substrate in the reaction was carried out. The slope of each fluorescence curve from 0 to 10 min was calculated as the velocity of the corresponding reaction. Three independent experiments were performed. The data were analyzed using a four-parameters model in GraphPad Prism 9 software to obtain the IC_{50} values of WU-04 and Ensitrelvir.

To measure the K_i values of Nirmatrelvir, 10 μL of Nirmatrelvir at a series of concentrations in the dilution buffer (20 mM HEPES 7.4, 150 mM NaCl, 0.01% Triton X-100, 1 mM DTT, 10% DMSO) was incubated with 20 μL of the fluorogenic substrate (50 μM) in the reaction buffer at 37 °C for 5 min. Then, 10 μL of 3CLpro (100 nM) in the reaction buffer (20 mM HEPES 7.4, 150 mM NaCl, 0.01% Triton X-100, 1 mM DTT) was added to each well to initiate the proteolytic reaction. The K_i was calculated by plotting the initial velocity against the concentration of Nirmatrelvir using the Morrison K_i plot in Prism 9 software.

ITC

ITC experiments were done with the isothermal titration calorimeter MicroCal PEAQ-ITC (Malvern Panalytical). 20 μM of WU-04 in the ITC buffer (20 mM HEPES, pH 7.4, 150 mM NaCl, 0.5% DMSO) was titrated by 200 μM of 3CLpros in the ITC buffer at 25 °C. The data were processed using the MicroCal PEAQ-ITC analysis software.

Crystallization

The SARS-CoV-2 3CLpro mutants were concentrated to 10 mg/mL, followed by centrifugation at 21,000× *g* for 5 min to remove the precipitate. DTT was added to a final concentration of 5 mM before crystallization for M49K/S301P. For crystallization, 0.2 μL of the protein was mixed with 0.2 μL of well buffer in a 96-well plate by a protein crystallization robot (Mosquito) using the sitting drop method (M165V and S301P) or hanging drop method (M49K, M49K/165V and M49K/S301P), then the drop was equilibrated against 90 μL of the well buffer at 20 °C. The well buffer for the crystallization of the M49K mutant contained 0.2 M BIS-TRIS, pH 6.0, 20% w/v polyethylene glycol 4000. The well buffer for the crystallization of the M165V mutant contained 0.2 M BICINE, pH 8.1, 20% polyethylene glycol 4000. The well buffer for the crystallization of the S301P mutant contained 0.2 M BIS-TRIS, pH 6.6, 20% polyethylene glycol 4000. The well buffer for the crystallization of the M49K/M165V double mutant contained 0.2 M BIS-TRIS propane, pH 7.3, 20% polyethylene glycol 4000. The well buffer for the crystallization of the M49K/S301P double mutant contained 0.2 M LiSO4, 0.1 M BIS-TRIS, pH 6.6, 17.5% polyethylene glycol 3350. The complex of the M49K/S301P double mutant with WU-04 was prepared by incubating the M49K/S301P double mutant (10 mg/mL in 20 mM HEPES, pH7.4, 150 mM NaCl) with 1.5 mM WU-04 (the stock used is 50 mM in DMSO) at room temperature for 2 h, followed by centrifugation at 21,000× *g* for 5 min to remove the precipitate. Then, 0.2 μL of the complex was mixed with 0.2 μL of the well buffer in a 96-well plate using the sitting drop method and the drop was equilibrated against 90 μL of the well buffer at 20 °C. The well buffer contains 0.1 M sodium formate, 12% polyethylene glycol 3350.

Data collection and structure determination

The crystals were first transferred to a cryoprotectant solution (the well buffer plus 20 mM HEPES, pH 7.4, 150 mM NaCl, and 10%–20% glycerol), then loaded onto the X-ray diffractometer (Rigaku, XtaLAB Synergy Customer) at Westlake University. The diffraction data were collected at 100 K and processed with the reduction program CrysAlisPro. The structures were solved by molecular replacement using Phaser in PHENIX[31]. The co-crystal structure of SARS-CoV-2 3CLpro/WU-04 (PDB code: 7EN8) was used as the initial model. The structures were manually refined with Coot and PHENIX[32]. Data collection and refinement statistics can be found in Supplementary Table S2 that were generated using the utility PHenix.table_one in PHENIX[33].

BRET-based cell assay

The BRET assay was performed following a method described previously[27]. Briefly, HEK 293 T cells were seeded into a 96-well clear-bottom white plate (Corning, 3903) at ~40% confluence. After 24 h, the cells were transfected with plasmids carrying the biosensors (400 ng/well) using PEI as the transfection reagent. Then, 3CLpro inhibitors with a series of concentrations in DMSO were added to the cell culture. The well with the HEK 293 T cells transfected with an empty plasmid and treated with DMSO was used as a blank control. The final concentration of DMSO in the cell culture was 0.48%. 24 h post transfection, coelenterazine 400a (GoldBio, C-320) was added to reach a final concentration of 10 μM and the

luminescence at 413 nm (wavelength range from 400 nm to 425 nm) and fluorescence at 518 nm (wavelength range from 505 nm to 530 nm) were measured after shaking for 5 s using a plate reader (TECAN-Spark). The BRET ratio was calculated using the following equation:

$$\text{BRET ratio} = (F_{518,S} - F_{518,BLK})/(L_{413,S} - L_{413,BLK})$$

in which $F_{518,\ S}$ and $L_{413,\ S}$ are the fluorescence (518 nm) and luminescence (413 nm) signals of cells, respectively, while $F_{518,\ BLK}$ and $L_{413,\ BLK}$ are the fluorescence (518 nm) and luminescence (413 nm) signals of the blank control, respectively.

MP

MP experiments[22] were performed using Refeyn TwoMP instruments (Refeyn Ltd.). The microscope coverslips (Thorlabs) were assembled into the flow chamber, and silicone gaskets (Grace Bio-Labs) were placed on the glass surface for sample loading to accommodate the sample drops with 3 × 2 wells prior to measurements. Contrast-to-mass calibration was achieved by measuring the contrast of BSA (Sigma-Aldrich, A1933), thyroglobulin (Sigma-Aldrich, 609312), and beta-amylase (Sigma-Aldrich, A7130) mixtures. The calibration curve with an R^2 value of 0.999 and a maximum mass error of 5.5% was fitted in Refeyn DiscoverMP software. The calibration was applied to each sample measurement to calculate the molecular mass of each histogram distribution during the analysis. The WT 3CLpro and its mutants in 20 mM HEPES pH 7.4, 150 mM NaCl, were diluted in the working buffer (20 mM HEPES pH 7.4, 150 mM NaCl) to the final concentration of 100 nM. Prior to sample analysis, 18 μL of fresh working buffer (20 mM HEPES pH 7.4, 150 mM NaCl) adjusted to room temperature was pipetted into a well to find the focal position, which was identified and locked in using the autofocus function of the instrument. For each acquisition, 2 μL of the diluted protein samples were added to the well and thoroughly mixed, and movies of 60 s duration (6000 frames) were recorded per measurement using Refeyn AcquireMP using regular image acquisition mode. The data were processed and analyzed by Refeyn DiscoverMP, then each histogram was fitted with Gaussian distribution to determine the mass (kDa) and normalized counts. Then the dissociation constant (K_d) values were calculated following the method described previously[34]. The mean and standard deviation of the K_d of the WT 3CLpro and each of its mutants were calculated with the K_d values from three measurements.

MD simulations and analysis

MD simulations were carried out using OpenMM 7.7.0[35]. The 3CLpro dimer was solvated in a cubic box of 104 Å, with protein modeled by the CHARMM36m force field[36]. The TIP3P model was employed to explicitly describe the water molecules, and a salt concentration of 0.15 M NaCl was incorporated using the CHARMM c47b1[37]. Nonbond interactions were truncated using a cutoff of 12 Å, with a switch function starting at 10 Å. Long-range electrostatic interactions were treated by the particle-mesh Ewald (PME) method. Each system underwent minimization and equilibration in the NVT ensemble for 300 ps, followed by NPT equilibration for 1 ns. The production runs were carried out in the NPT ensemble with a temperature of 310.15 K and a pressure of 1 bar. Pressure control was achieved using the Monte Carlo barostat, while integration and temperature control were performed using the Langevin integrator with a friction coefficient of 1 ps^{-1}. All bonds involving hydrogen atoms were constrained. MM/GBSA calculations were performed using frames extracted at 1 ns interval from the MD trajectories.

Thermal shift assay

The thermal shift assay was performed in the BIO-RAD CFX Connect Real-Time PCR Detection System. To 10 μL of 3CLpro (10 μM) in 20 mM HEPES, pH 7.4, 150 mM NaCl in a 96-well PCR plate (BIO-RAD MLL9601), 10 μL of 10× SYPRO™ Orange in the reaction buffer (20 mM HEPES, pH 7.4, 150 mM NaCl, 2 mM DTT, 0.02% Triton X-100) was added and mixed gently. The final reaction contained 5 μM of 3CLpro, 5× SYPRO™ Orange, 20 mM HEPES, pH 7.4, 150 mM NaCl, 1 mM DTT, 0.01% Triton X-100. The reaction buffer plus SYPRO™ Orange was used as no protein control. The fluorescence was monitored under a temperature gradient ranging from 25 °C to 95 °C in 0.5 °C increments every 30 s after an initial incubation at 25 °C for 5 min. Each data set was normalized to the highest fluorescence, and the normalized fluorescence reading was plotted against temperature in GraphPad Prism 9. The melting temperature (T_m) values were determined as the temperature corresponding to the maximum of the first derivative of the curve. The melting temperature shift (ΔT_m) of 3CLpro mutants was calculated by subtracting the T_m of the WT 3CLpro.

Acknowledgements

We thank Dr. Sheng-ce Tao at Shanghai Jiao Tong University for sharing the plasmids of SARS-CoV-2 proteins. We thank the Protein Characterization and Crystallography Facility of Westlake University for assistance in crystallization and X-ray data collection. We thank Shan Feng and Jinheng Pan at the Mass Spectrometry & Metabolomics Core Facility of Westlake University for their technical assistance. We would like to express our sincere gratitude towards Tencent Foundation for their generous support in this collaborative project. This work was supported by "Pioneer" and "Leading Goose" R&D Program of Zhejiang (2023C03109, 2024SSYS0036), Changping Laboratory (2021A-06-02), Central Guidance on Local Science and Technology Development Fund (2022ZY1006), Westlake Education Foundation, and Tencent Foundation.

Author details
[1]Zhejiang University, Hangzhou, Zhejiang, China. [2]Westlake Laboratory of Life Sciences and Biomedicine, Hangzhou, Zhejiang, China. [3]School of Life Sciences, Westlake University, Hangzhou, Zhejiang, China. [4]Institute of Biology, Westlake Institute for Advanced Study, Hangzhou, Zhejiang, China. [5]Department of Biochemistry and Molecular Biology, University of Texas Medical Branch, Galveston, TX, USA. [6]Division of Life Sciences and Medicine, University of Science and Technology of China, Hefei, Anhui, China. [7]Changping Laboratory, Yard 28, Science Park Road, Changping District, Beijing, China

Author contributions
Q.H. conceived the project. L.Z. designed and performed the biochemical assays. L.Z. and H.L. purified the proteins and did the crystallization experiments. Q.H. and L.Z. determined and refined the crystal structures. X.X. and P.Y.S. performed the virology experiments. Y.Y. performed the MP experiments and L.Z. analyzed the data. J.H. and R.Q. did the MD simulations. All the authors analyzed the data. L.Z. and Q.H. wrote the manuscript with inputs from other authors.

Data availability
All data and materials presented in this manuscript are available from the corresponding author (Q.H.) upon a reasonable request under a completed Materials Transfer Agreement (MTA). The crystal structures have been deposited in the Protein Data Bank (www.rcsb.org) with the accession numbers 8K68 (the M49K mutant), 8K67 (the M165V mutant), 8K6A (the S301P mutant), 8K6B (the M49K/M165V mutant), 8K6C (the M49K/S301P mutant), and 8K6D (the M49K/S301P mutant in complex with WU-04). All other data are available in the manuscript or the supplementary materials.

Conflict of interest
L.Z., H.Y., J.H., and Q.H. are co-inventors of patents that cover the 3CLpro inhibitor WU-04 in this study. H.Y., J.H., and Q.H. are founders of Westlake Pharmaceuticals (Hangzhou) Co., Ltd. and members of its scientific advisory board. Other authors declare no competing interests.

Supplementary information The online version contains supplementary material available at https://doi.org/10.1038/s41421-024-00673-0.

Received: 6 November 2023 Accepted: 27 March 2024
Published online: 09 April 2024

References

1. Fehr, A. R. & Perlman, S. Coronaviruses: an overview of their replication and pathogenesis. *Methods Mol. Biol.* **1282**, 1–23 (2015).
2. Zhou, P. et al. A pneumonia outbreak associated with a new coronavirus of probable bat origin. *Nature* **579**, 270–273 (2020).
3. Coronaviridae Study Group of the International Committee on Taxonomy of, V. The species Severe acute respiratory syndrome-related coronavirus: classifying 2019-nCoV and naming it SARS-CoV-2. *Nat. Microbiol.* **5**, 536–544 (2020).
4. Owen, D. R. et al. An oral SARS-CoV-2 M(pro) inhibitor clinical candidate for the treatment of COVID-19. *Science* **374**, 1586–1593 (2021).
5. Jiang, X. et al. Structure-based development and preclinical evaluation of the SARS-CoV-2 3C-like protease inhibitor simnotrelvir. *Nat. Commun.* **14**, 6463 (2023).
6. Chen, X. et al. Preclinical evaluation of the SARS-CoV-2 M^{pro} inhibitor RAY1216 shows improved pharmacokinetics compared with nirmatrelvir. *Nat. Microbiol.* https://doi.org/10.1038/s41564-024-01618-9 (2024).
7. Unoh, Y. et al. Discovery of S-217622, a noncovalent oral SARS-CoV-2 3CL protease inhibitor clinical candidate for treating COVID-19. *J. Med. Chem.* **65**, 6499–6512 (2022).
8. Ou, J. et al. A yeast-based system to study SARS-CoV-2 M^{pro} structure and to identify nirmatrelvir resistant mutations. *PLoS Pathog.* **19**, e1011592 (2023).
9. Jochmans, D. et al. The substitutions L50F, E166A, and L167F in SARS-CoV-2 3CLpro are selected by a protease inhibitor in vitro and confer resistance to nirmatrelvir. *mBio* **14**, e0281522 (2023).
10. Iketani, S. et al. Multiple pathways for SARS-CoV-2 resistance to nirmatrelvir. *Nature* **613**, 558–564 (2023).
11. Zhou, Y. et al. Nirmatrelvir-resistant SARS-CoV-2 variants with high fitness in an infectious cell culture system. *Sci. Adv.* **8**, eadd7197 (2022).
12. Hu, Y. et al. Naturally occurring mutations of SARS-CoV-2 main protease confer drug resistance to nirmatrelvir. *ACS Cent. Sci.* **9**, 1658–1669 (2023).
13. Sasi, V. M. et al. Predicting antiviral resistance mutations in SARS-CoV-2 main protease with computational and experimental screening. *Biochemistry* **61**, 2495–2505 (2022).
14. Yang, K. S., Leeuwon, S. Z., Xu, S. & Liu, W. R. Evolutionary and structural insights about potential SARS-CoV-2 evasion of nirmatrelvir. *J. Med. Chem.* **65**, 8686–8698 (2022).
15. Iketani, S. et al. Functional map of SARS-CoV-2 3CL protease reveals tolerant and immutable sites. *Cell Host Microbe* **30**, 1354–1362.e6 (2022).
16. Heilmann, E. et al. SARS-CoV-2 3CL(pro) mutations selected in a VSV-based system confer resistance to nirmatrelvir, ensitrelvir, and GC376. *Sci. Transl. Med.* **15**, eabq7360 (2023).
17. Moghadasi, S. A. et al. Transmissible SARS-CoV-2 variants with resistance to clinical protease inhibitors. *Sci. Adv.* **9**, eade8778 (2023).
18. Noske, G. D. et al. Structural basis of nirmatrelvir and ensitrelvir activity against naturally occurring polymorphisms of the SARS-CoV-2 main protease. *J. Biol. Chem.* **299**, 103004 (2023).
19. Flynn, J. M. et al. Systematic analyses of the resistance potential of drugs targeting SARS-CoV-2 main protease. *ACS Infect. Dis.* **9**, 1372–1386 (2023).
20. Duan, Y. et al. Molecular mechanisms of SARS-CoV-2 resistance to nirmatrelvir. *Nature* **622**, 376–382 (2023).
21. Hou, N. et al. Development of highly potent noncovalent inhibitors of SARS-CoV-2 3CLpro. *ACS Cent. Sci.* **9**, 217–227 (2023).
22. Young, G. et al. Quantitative mass imaging of single biological macromolecules. *Science* **360**, 423–427 (2018).
23. Bjorkman, P. et al. Design of wide-spectrum inhibitors targeting coronavirus main proteases. *PLoS Biol.* **3**, e324 (2005).
24. Kiso, M. et al. In vitro and in vivo characterization of SARS-CoV-2 resistance to ensitrelvir. *Nat Commun* **14**, 4231 (2023).
25. Kiso, M. et al. In vitro and in vivo characterization of SARS-CoV-2 strains resistant to nirmatrelvir. *Nat. Commun.* **14**, 3952 (2023).
26. Niesen, F. H., Berglund, H. & Vedadi, M. The use of differential scanning fluorimetry to detect ligand interactions that promote protein stability. *Nat. Protoc.* **2**, 2212–2221 (2007).
27. Hou, N., Peng, C., Zhang, L., Zhu, Y. & Hu, Q. BRET-based self-cleaving biosensors for SARS-CoV-2 3CLpro inhibitor discovery. *Microbiol. Spectr.* **10**, e0255921 (2022).
28. Abdelnabi, R. et al. Nirmatrelvir-resistant SARS-CoV-2 is efficiently transmitted in female Syrian hamsters and retains partial susceptibility to treatment. *Nat. Commun.* **14**, 2124 (2023).
29. Johnson, B. A. et al. Nucleocapsid mutations in SARS-CoV-2 augment replication and pathogenesis. *PLoS Pathog.* **18**, e1010627 (2022).
30. Xie, X. et al. An Infectious cDNA clone of SARS-CoV-2. *Cell Host Microbe* **27**, 841–848 e843 (2020).
31. McCoy, A. J. et al. Phaser crystallographic software. *J. Appl. Crystallogr.* **40**, 658–674 (2007).
32. Emsley, P., Lohkamp, B., Scott, W. G. & Cowtan, K. Features and development of Coot. *Acta Crystallogr. D Biol. Crystallogr.* **66**, 486–501 (2010).
33. Liebschner, D. et al. Macromolecular structure determination using X-rays, neutrons and electrons: recent developments in Phenix. *Acta Crystallogr. D Struct. Biol.* **75**, 861–877 (2019).
34. Soltermann, F. et al. Quantifying protein-protein interactions by molecular counting with mass photometry. *Angew. Chem. Int. Ed. Engl.* **59**, 10774–10779 (2020).
35. Eastman, P. et al. OpenMM 7: rapid development of high performance algorithms for molecular dynamics. *PLoS Comput. Biol.* **13**, e1005659 (2017).
36. Huang, J. et al. CHARMM36m: an improved force field for folded and intrinsically disordered proteins. *Nat. Methods* **14**, 71–73 (2017).
37. Brooks, B. R. et al. CHARMM: the biomolecular simulation program. *J. Comput. Chem.* **30**, 1545–1614 (2009).